Philosophical Magazine
2011, 1–25, iFirst

Energy barriers associated with slip–twin interactions

Tawhid Ezaz, Michael D. Sangid and Huseyin Sehitoglu*

Department of Mechanical Science and Engineering, University of Illinois at Urbana-Champaign, 1206 W. Green St., Urbana, IL 61801, USA

(*Received 1 June 2010; final version received 12 November 2010*)

The energetics of slip–coherent twin boundary (CTB) interactions are established under tensile deformation in face centered cubic (fcc) copper with molecular dynamics simulations, exploring the entire stereographic triangle. The CTBs serve as effective barriers in some crystal orientations more than others, consistent with experimental observations. The resulting dislocation structures upon slip–twin reactions are identified in terms of Burgers vector analysis. Visualization of the dislocation transmission, lock formation, dislocation incorporation to twin boundaries, dislocation multiplication at the matrix–twin interface and twin translation, growth, and contraction behaviors cover the most significant reactions that can physically occur providing a deeper understanding of the mechanical behavior of fcc alloys in the presence of twin boundaries. The results make a distinction between deformation and annealing twins interacting with incident dislocations and point to the considerable role both types of twins can play in strengthening of fcc metals.

Keywords: twinning; molecular dynamics; copper; slip; dislocations; energy; energy barrier; twin boundary

1. Introduction

Since the early observations of twinning in face centered cubic (fcc) materials [1], there have been numerous research studies on characterizing slip–coherent twin boundary interactions. These interactions have a profound influence on the mechanical behavior of fcc metals and alloys [2–5] with high strain-hardening coefficients and strong crystallographic orientation dependence [2–4,6–8]. The issue of slip–coherent twin boundary (CTB) reactions is complex because, depending on the loading axis with respect to the slip system, dislocations with different partial separation distances [9] and screw versus edge components are activated. In these reactions, the incident leading dislocation is of $\langle 11\bar{2}\rangle\{111\}$ type; the outgoing dislocation can take various planes and directions with residual dislocations forming based on the reactions at the CTB. The trailing partial can facilitate dislocation multiplication at the CTB upon interaction with the residual dislocations. The planar fault energies are modified depending on the internal stress fields; for example, due to stair rod and Frank partial dislocations, and, in some cases, the CTB acts as a source for dislocation multiplication. Our aim is to quantify the energetics of

*Corresponding author. Email: huseyin@illinois.edu

ISSN 1478–6435 print/ISSN 1478–6443 online

DOI: 10.1080/14786435.2010.541166
http://www.informaworld.com

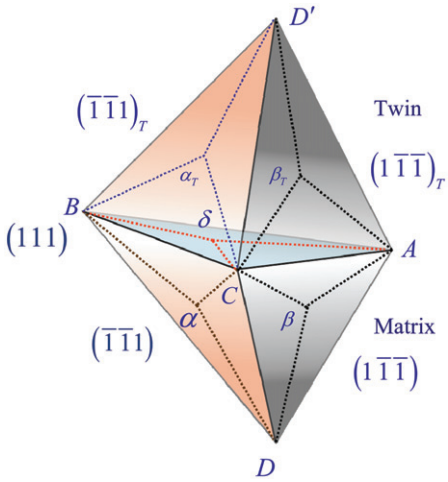

Figure 1. Double Thompson's tetrahedron for the twin–matrix orientation relationship. The (111) or δ is the coherent twin plane. The twinned directions and planes are expressed with a subscript T. Here, $B\delta = [\bar{2}11](111)$, $D\beta = [211](1\bar{1}\bar{1})$, and $\beta_T D' = [211]_T(1\bar{1}\bar{1})_T$.

dislocation glide in the presence of slip–twin interactions revealing the crystallographic loading orientation dependence.

The reactions involving partial dislocations can be best understood with the double Thompson tetrahedron. A double tetrahedron representation of the twin–matrix system configuration is shown in Figure 1 [10]. In this representation, δ or (111) is the twin plane, α, β, γ and $\alpha_T, \beta_T, \gamma_T$ represent the glide planes for partial dislocations in the matrix and twin, respectively. For instance, β represents the $(1\bar{1}\bar{1})$ plane in the matrix and β_T characterizes the $(1\bar{1}\bar{1})_T$ glide plane in the twin. It is noted that the coherent twin boundaries (deformation and annealing types) are a special type of grain boundary, classified with a high degree of coincidence, $\Sigma = 3$, where Σ denotes the ratio of the volume of coincidence site lattice to the regular lattice.

The interaction of incident dislocations with CTB can result in incorporation [11–15] on the δ plane, transmission following incorporation [16–20] on the $\alpha_T, \beta_T, \gamma_T$ planes, or glide plane transmission [17,21–24] on the $\alpha_T, \beta_T, \gamma_T$ planes. Short-range transmission on cube planes can occur when the other slip systems are not available [25–28]. In addition, the incident dislocation–CTB reactions can also trigger dislocation multiplication [10,13,18,19,29] on α, α_T planes and twin translation [30,31] on the δ plane; these represent two mechanisms that are not well studied. The culmination of these cases underscores the complexity of dislocation–CTB interactions that need to be considered on a case-by-case basis. The Burgers vector reactions for these mechanisms can be devised based on the Thompson tetrahedra. However, the energy barriers associated with glide are influenced by the reaction, specifically stair rod dislocation of sessile configurations, locks, and Frank dislocations at the twin boundaries analogous to those that form inside the grains, which require further calculation as we consider in this work.

During the incorporation process (Figure 2a, Case (i)), the leading partial on any of the α, β, γ planes (shown with brown arrow; the coloring is consistent with the

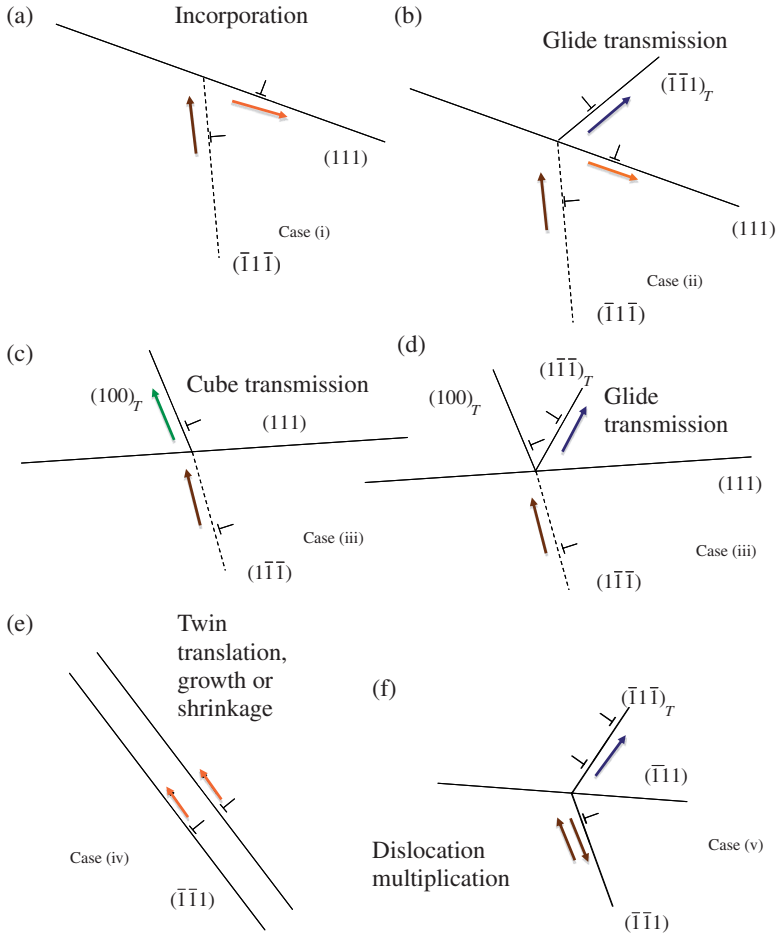

Figure 2. Schematic of most significant dislocation –twin interactions: Case (i) is depicted in (a), Case (ii) in (b), Case (iii) in (c) and (d), Case (iv) in (e), and Case (v) in (f). Coloring of the arrows is consistent with the double Thompson tetrahedra. See text for details.

arrows in Thompson double tetrahedra shown later for each case) impinges at the CTB (δ). Then, a twinning partial nucleates and glides along the CTB (shown with orange arrow). Therefore, the incident dislocation is incorporated in the twin by transverse (or lateral) growth as illustrated in Figure 2a. In general, the dislocation–twin boundary reactions can result in both twin shrinkage [12] or twin growth depending on the direction of the twinning partial in the twin plane [19]. The following additional interactions can develop at the CTB. Case (ii): {111} glide plane (glide plane transmission, $\alpha_T, \beta_T, \gamma_T$; Figure 2b); this is the case of transmission (shown with blue arrow) following dislocation incorporation. Case (iii): short-range {100} cube transmission (shown with green arrow) and {111} glide (Figures 2c and d, respectively). Glide transmission follows from the reaction of trailing partial with a residual dislocation in Case (iii) [12,13,19], with elevated energy barriers for glide transmission (Figure 2d), as we will see later. In addition to the aforementioned

reactions, CTB translations can occur (Case (iv), Figure 2e), which move the upper and lower twin–matrix interfaces in the transverse direction [30–35]. An important ramification of the incorporation and transmission processes is that several dislocation multiplication (nucleation) events can occur at the interaction site [10,13,18,19,29] (Case (v), Figure 2f). By dislocation multiplication (Case (v)), we mean remission into the matrix (double brown arrow indicates incident and reemitted) and new dislocation generation in the twin. This multiplication process (illustrated in Figure 2f) is governed by the type of the incident dislocation [36] and the magnitude of the Schmid factor [21]. Nucleation of a perfect dislocation in the twin and a partial in the matrix occurs; meanwhile, a twinning partial is incorporated in the CTB [19] in this case.

A noteworthy outcome of slip–twin interaction is that a mixed or perfect edge dislocation leaves a residual dislocation at the CTB. The residual dislocation significantly elevates the local stresses and energy barrier for dislocation nucleation at the CTB. However, a perfect screw dislocation can be incorporated within the twin boundary or transmitted via a cross-slip process without any residual dislocation at the CTB [37–39]. The only energy barrier that a screw dislocation needs to overcome is the elastic mismatch and distortion of the deformation field [40]. Hence, screw dislocation–CTB reaction contribution is expected to be small compared to the cases studied here.

The types of twins seen under the microscope prior to external loading are termed annealing or growth twins [41]. A distinction is noteworthy among the deformation twins and the annealing/growth (non-deformation) twins in fcc metals. The deformation twins are formed under the prevailing stress state (loading direction) in the material. The non-deformation twins are also on the {111} planes, but would not necessarily be favorable for further growth under the given loading orientation. To achieve a complete understanding of twin–slip encounters, one needs to study the pre-existing non-deformation twin cases as well. Recent works on nanocrystals [27,28] point to additional strengthening in the [111] loading orientation due to the presence of nanoscale non-deformation twins. We show this as a special case and explore its energy barrier. The primary contribution of this work is to develop a unique methodology for tracking short-range planar fault energies in the vicinity of CTBs.

Dislocation–CTB interactions involve complex dislocation reactions with the underlying physics at the atomic length scale, so continuum dislocation theory has limitations in descriptions at this level. Experimental techniques cannot easily provide dynamic evolution information and also cannot reveal unstable states (such as the unstable stacking fault energies). We devise a special method for tracking the energy of atoms during the deformation, and the results reproduce the baseline generalized stacking fault energy (GSFE) curves as a limiting case under 'static' conditions. We provide a brief overview of GSFE and generalized planar fault energy (GPFE) in Section 2.

In summary, it is evident through previous knowledge that the loading orientation, type of incident dislocation (screw and edge components) and the Schmid factor at the CTB influence the dislocation–CTB interaction. Despite numerous investigations on twin–slip interactions, we cannot, *a priori*, predict the outcome of the reaction. The present study is aimed at identifying the dislocation–CTB interactions through a systematic investigation with the help of a Burgers circuit analysis, detailed identification of slip–twin planes/directions and the energetics of the dislocation

glide, thereby identifying the energy barriers corresponding to dislocation motion as a function of the underlying screw and edge components of the incident dislocation. A unifying treatment of the most significant CTB–slip interaction scenarios is needed to assist with modeling efforts and to put the observations into a generalized framework. This paper will focus on addressing this need.

2. Methods

2.1. *Description of GSFE and GPFE*

The GSFE is the interplanar potential energy required to slide one elastic half space of the crystal relative to the other along the {111} glide plane in the ⟨112⟩ slip direction [42]. The schematic GSFE and GPFE curves are illustrated in Figure 3a. The first peak in this energy curve is termed the unstable stacking fault energy (γ_{US}) associated with the leading partial. The stable configuration is known as the intrinsic stacking fault energy (γ_{isf}), corresponding to the normalized displacement (reaction coordinate) equalling one. The GPFE portrays the twin fault energy by extending the energy barrier from the intrinsic stacking fault to a finite number of twin layers. Thus, a GPFE calculation requires shearing of consecutive {111} elastic planes along the ⟨112⟩ direction relative to the pre-existing stacking fault or twin. A GPFE curve is characterized (in addition to the γ_{US}, γ_{isf} mentioned above) by the magnitudes of unstable twin energies (γ_{UT}) and stable twin energies ($2\gamma_{tsf}$).

The solid line in Figure 3a represents the planar fault energy curve under a stress field. In this study, the short-range planar fault energy near the CTB is determined dynamically alongside the conventional molecular statics method. In the case of dislocation multiplication at the CTB, the dislocation experiences a higher $\gamma_{US-unrelax}$ compared to the baseline γ_{US} peak. For the case of incorporation of the incoming dislocation at the CTB, the curve peaks at $\gamma_{UT-unrelax}$ compared to the baseline γ_{UT} peak. The unrelaxed energies approach the relaxed curves as one moves away from the local stress field created by sessile dislocations at the CTB. We note that the GSFE curve for the trailing partial γ_{US} is the same as the leading in a perfect lattice, while the $\gamma_{US-unrelax}$ associated with the trailing may differ due to the presence of the reactions and residual dislocations at the CTB.

2.2. *Simulation procedures*

The EAM potential for Cu developed by Mishin et al. [43] provides planar fault energies in good agreement with the values provided by density functional theory [44,45]; hence, this potential is selected for this study. As stated earlier, calculations of planar fault energy curves are conducted with both molecular statics and a dynamical method in this current study. During energy minimization in the statics method, the atoms are relaxed partially in the ⟨111⟩ direction but no relaxation is allowed in the $\langle\bar{2}11\rangle$ or $\langle 0\bar{1}1\rangle$ directions, thus fixing the positions of the atoms in these directions. This is essential to maintain the atoms at their relevant positions, otherwise the atoms move to stable energy positions near the fault during relaxation. The energy barrier is then calculated comparing the total internal energy of the crystal with lattice misfit to that of a perfect fcc crystal. The relaxed results obtained

by molecular statics are designated as the baseline GSFE or GPFE in this paper. For Cu, the magnitudes of γ_{US} and γ_{isf} are calculated to be 167 and 44 mJ m^{-2} in the current study. These magnitudes are consistent with *ab initio* calculations. For Cu, the magnitude of γ_{UT} is calculated as 187 mJ m^{-2} consistent with *ab initio* results [45], and we note that $2\gamma_{tsf} \approx \gamma_{isf}$.

During the molecular dynamics (MD) based short range planar energy calculation near the twin boundary, fixation of atoms in any particular direction is not enforced as the motion of the atoms during dislocation nucleation is reaction

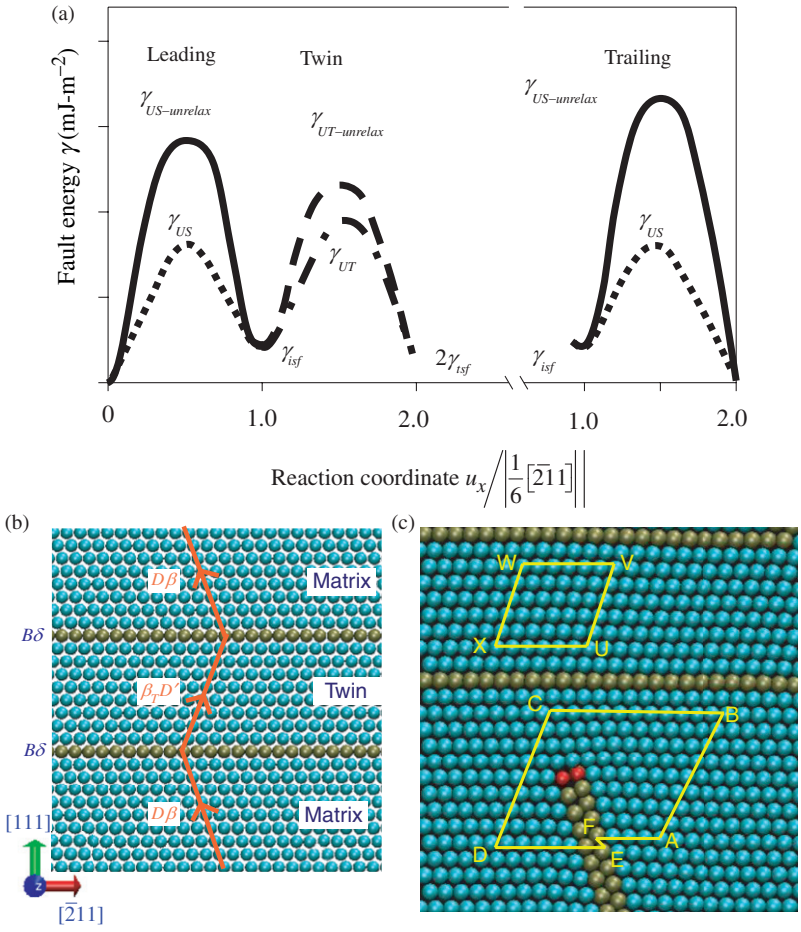

Figure 3. (a) Schematic of the generalized stacking fault energy (GSFE) and generalized planar fault energy (GPFE) curves, illustrating the position of the barriers and energy wells that the atoms glide through during its motion. Also, schematic of the unrelaxed GSFE exhibits the possible stress contribution in the curve. (b) Atomic structure of a matrix–twin–matrix configuration viewed from the $[01\bar{1}]$ direction. The line indicates the direction of a Shockley partial in the $\{111\}$ glide plane. (c) A Burgers circuit UVWX is drawn around a perfect fcc lattice, which exhibits perfect closure, whereas Burgers circuit ABCDEF drawn around a dislocation points out a closure misfit EF. Burgers vector confirms this dislocation is of $\frac{a}{6}[211]$ type, which is a leading partial in $(1\bar{1}\bar{1})$ plane.

path-dependent and follows the minimum energy direction in the closed packed plane. Both the potential energy and position of an array of atoms in the slip plane are monitored at a small timestep (0.01 fs). Energy barriers during dislocation nucleation and transmission are calculated from the potential energy difference between the lattices with defects and the perfect lattices at a particular time step.

Throughout the molecular statics and dynamics calculations, the temperature of the system is maintained at 10 K; hence, providing a consistent baseline. Internal energy fluctuation of the monitored atoms due to entropy is measured to be very small at this temperature – in the order of 0.0011 eV. The long-range hydrostatic stress field is removed from the energy calculation by comparing the energy of perfect fcc atoms under the same external stress field. This provides a consistent framework for comparison of different loading conditions in this study. Thus, any deviation for γ_{US} or γ_{UT} peak points to the effect of the internal stresses nearby the CTBs.

The MD simulation consists of a box of dimension $50 \times 50 \times 50$ nm with a 10 layer thick twin. The twin orientations for various loading conditions provide different twin Schmid factors for tension, as expected. Our aim is to explore all the significant possibilities of twin orientations to capture the prevailing twin–slip interaction scenarios. Table 1 shows the various twin systems employed in these simulations and their corresponding twin Schmid factors for different loading (lattice) orientations. For a particular loading direction, only the twin systems with maximum or minimum twin Schmid factor are presented, as discussed in Section 3, although all twin systems are analyzed. Figure 3b displays the atomic structure of a matrix–twin configuration loaded in the [111] direction. The {111} glide planes in the matrix and twin are shown and the CTB atoms are colored differently than the matrix.

A parallel molecular dynamics program, LAMMPS [46], is used for both molecular statics and dynamics calculation. The atoms are first equilibrated statically to maintain a minimum energy configuration using the conjugate gradient method. This ensures a stress free crystal prior to loading. During dynamic loading, uniaxial tension is applied up to 15% engineering strain at a strain rate of $10^9\,s^{-1}$. The high strain rate is inherent in the simulations for computational efficiency to have the desired amount of deformation within a given simulation time. An NPT ensemble

Table 1. Twin systems and the corresponding Schmid factor of the twin boundary and the incident dislocation in different loading orientation, where $(lmn)[pqr]$ represents a matrix crystallographic orientation of x $[pqr]$, y $[lmn]$, z $[pqr \times lmn]$. Non-deformation twins are indicated.

Loading orientation (Tension)	Twin system $(lmn)[pqr]$	Twin Schmid factor	Schmid factor for incident dislocation
[010]	$(1\bar{1}1)[\bar{2}11]$	0.24	0.24
[111]	$(1\bar{1}\bar{1})[\bar{1}2\bar{1}]$	0.31	0.31
[111]	$(1\bar{1}1)[\bar{2}11]$	0.0[a]	0.31
[101]	$(1\bar{1}\bar{1})[121]$	0.47	0.47
[321]	$(\bar{1}11)[112]$	0.47	0.47
[321]	$(\bar{1}11)[211]$	0.0[a]	0.47

Note: [a]Non-deformation twins.

is utilized during the dynamic deformation where the number of atoms in the simulation box, N, the pressure/stress in the three directions, P, and the system temperature, T, are held constant throughout the simulation.

The simulation box is created with the $(lmn)\langle pqr\rangle$ twin system, as outlined in Table 1, maintaining periodic boundary condition in all three directions. The system is then rotated to the appropriate loading direction and subjected to a uniaxial tension loading. The matrix and the twin descriptions are consistent with the Thompson tetrahedra described in Figure 1 earlier. For cases when periodicity cannot be invoked due to the geometry of twin boundaries, we ensure that the box size is chosen to achieve convergence of results without effects from the free surfaces. The atomic positions, reactions and the energetics are explored circumventing effects from the box size, image forces and free surfaces on the reactions and energy levels. In particular, the twin lengths are long compared to the finite domains, where slip–twin interactions occur.

We note that the presence of the void in the matrix ensured the nucleation of the incident dislocation at a stress magnitude considerably lower than in defect-free single crystal copper. The glide of the partial dislocation occurred at stress levels below 2 GPa depending on the loading orientation. The dislocation–CTB reactions and energy barriers are checked by conducting simulations with 3,5, 10, 20 and 100 atomic layers yielding the same results for all these cases.

2.3. *Visualization of results*

Special codes are written to visualize the details of the dislocation–CTB interactions with visual molecular dynamics (VMD) [47], an atomistic configuration viewer program. In the images of the simulation cell (Figure 3c), the centro-symmetry parameter is utilized [48]. Using this parameter, atoms which do not participate in the active slip processes are deleted to aid in visualizing the pertinent defects. The color red is assigned to partial dislocations, while stacking faults and twin boundaries are denoted in gold. Only the slip–CTB intersections are focused in the figures for a clear comprehension.

To obtain an estimate of the magnitude and direction of the dislocations, a special code for determining the Burgers vector is developed, which relies on an array of translational vectors that help to draw a Burgers circuit around the dislocation as illustrated in Figure 3c. Note that the non-closure of the circuit reveals the dislocation types reported in this work. Particularly revealing are the magnitudes of the glissile and sessile dislocations and their edge and screw components.

3. Results

Figure 4 illustrates the position of the loading directions in a stereographic triangle along with the Schmid factors for the twin systems in tension. These loading directions are carefully selected based on the relative resolved shear stress on the leading and trailing partials of the incident dislocations and the number of systems with maximum Schmid factor. A distinction is made based upon the Schmid factor of twin systems in a given loading direction. The twin system with the maximum

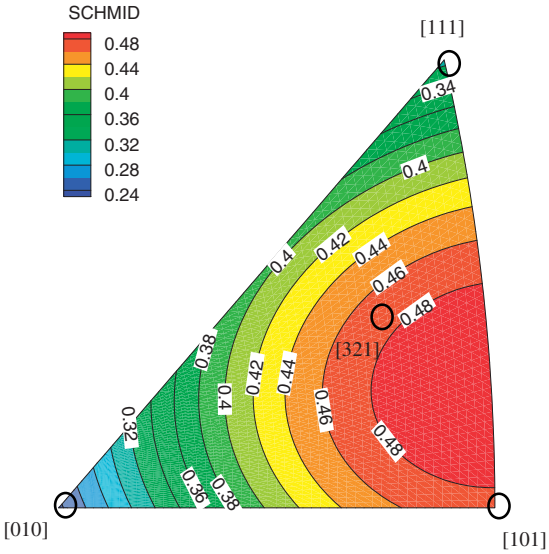

Figure 4. Schmid factor contours of the leading Shockley partials. Under tension, the leading Shockley partials serve as the twinning dislocations. The circles within the triangle display the position of the crystal loading direction analyzed in this paper.

Schmid factor for the leading partial is labelled as a 'deformation twin' in this study. Non-deformation twins can arise from previous loading/temperature history on the material, as previously discussed.

For the [010], [111], [101], and [321] crystal loading orientations loaded in tension, there are a total of 8, 3, 2 and 1 systems with the highest Schmid factor for the leading partial, respectively. We note that for the [010] loading, the trailing partial has a Schmid factor even higher than the leading, which inactivates this system. Therefore, for the [010] orientation, we consider 'non-deformation twins' only. Based on the loading orientations and type of twin, multiple categories of incident dislocation–CTB interactions are examined, which cover the most significant possibilities. Other stress states including compression (and the associated tension-compression asymmetry findings) and multi-axial stress states are not investigated in this current study. Different stress states would modify dislocation–CTB reactions; however, the basic concepts presented in this paper remain valid. The incident dislocations are nucleated from a stress concentrator (a void) sufficiently far from the CTB to negate stress field interactions, and this distance is systematically varied to ensure no size effects on the results. From this nucleation site, the dislocation glides and intersects with the CTB. Due to the incident dislocation nucleation from the void, the stress levels are lower than the ideal strength levels obtained from first principle calculations [49]. The incident dislocation varies between a mixed 60° dislocation, 30° partial and 90° partial dislocation depending upon the loading orientation within the crystal. Table 2 illustrates the screw and edge components of these incident dislocations observed during the dislocation CTB interaction, the reactions and the outgoing dislocations. In this study, we explore different regions of the stereographic triangle to categorize the dislocation–CTB interactions.

Table 2. Edge and screw components of the incident and outgoing dislocations for each case. Also, the residual dislocation type, summarizing the results as a function of lattice loading direction.

Loading orientation	Twin system	Incident leading dislocation	Outgoing dislocation	Residual dislocation	Interaction outcome	Components of incident leading dislocation	
						b_e	b_s
[010]	Deformation	$\frac{a}{6}[21\bar{1}](\bar{1}1\bar{1})$	$\frac{a}{6}[2\bar{1}\bar{1}](111)$	$\frac{a}{3}[010]$	Incorporation and transmission	$\frac{a}{2\sqrt{6}}$	$\frac{a}{2\sqrt{2}}$
[111]	Deformation	$\frac{a}{6}[112](1\bar{1}\bar{1})$	$\frac{a}{6}[12\bar{1}](1\bar{1}\bar{1})$	$\frac{a}{6}[0\bar{1}3]$	Incorporation and blockage	$\frac{a}{2\sqrt{6}}$	$\frac{a}{2\sqrt{2}}$
[111]	Non-deformation	$\frac{a}{6}[211](1\bar{1}\bar{1})$	$\frac{a}{2}[011]_T(100)_T$	$\frac{a}{6}[233]$*	Cube plane transmission	$\frac{a}{\sqrt{6}}$	0
[101]	Deformation	$[\bar{1}\bar{1}2](111)$	No interaction		Twin translation	$\frac{a}{\sqrt{6}}$	0
[321]	Deformation	$[112](11\bar{1})$	No interaction		Twin growth (or contraction)	$\frac{a}{\sqrt{6}}$	0
[321]	Non-deformation	$\frac{a}{6}[112](\bar{1}\bar{1}1)$	$\frac{a}{6}[121]_T(\bar{1}1\bar{1})_T$	$\frac{2a}{9}[\bar{1}11]$*	Transmission, multiplication (including remission)	$\frac{a}{2\sqrt{6}}$	$\frac{a}{2\sqrt{2}}$

Notes: *Further dissociation occurs.

3.1. *Dislocation transmission following CTB incorporation*

Upon tensile loading in the [010] crystal orientation, two mechanisms are operative. The incident dislocation reacts with a $(111)[\bar{2}11]$ CTB, which has the maximum twin Schmid factor for the [010] loading orientation. This is shown in Figure 5a, where a leading and trailing bowed partials are noted. A CTB incorporation of the incident dislocation results in transverse twin growth of the lamella followed by a transmission of the dislocation inside the twinned region (Figures 5b and c; Case (i) and (ii)). The CTB with the highest Schmid factor for the [010] loading is depicted in these figures, and the outgoing slip system also corresponds to the maximum resolved shear stress. The incident dislocation is a 60° mixed dislocation type with a 30° leading and a 90° trailing partial based on Burgers circuit analysis. The leading 30° partial glides in the $\frac{a}{6}[21\bar{1}]$ direction on the $(\bar{1}1\bar{1})$ plane as it leaves a widening intrinsic stacking fault behind. The Burgers vector of the dislocation is invariant along the dislocation line, although the character of dislocation changes along the dislocation front. At the line of intersection, the 30° leading partial is found to have screw and edge components of $\frac{a}{4}[10\bar{1}]$ and $\frac{a}{12}[121]$, respectively. This can be summarized in Equation (1):

$$\underbrace{\frac{a}{12}[121]}_{\text{Edge}} + \underbrace{\frac{a}{4}[101]}_{\text{Screw}} \rightarrow \underbrace{\frac{a}{6}[21\bar{1}]}_{30^\circ\text{ leading partial}} \quad . \tag{1}$$

A 90° trailing partial follows the leading partial as $\frac{a}{6}[121]$ $(\bar{1}1\bar{1})$ as noted in Figure 5a.

Once the 30° leading partial with a $\frac{a}{6}[21\bar{1}]$ Burgers vector is incorporated in the deformation CTB, the $\frac{a}{3}[010]$ type stair rod dislocation is generated along with a $\frac{a}{6}[2\bar{1}\bar{1}]$ twinning partial at the CTB (Figure 5b). The $\frac{a}{6}[\bar{2}11]_T(111)_T$ twin system has the maximum Schmid factor for the [010] loading direction and is thus favorable for glide. This twinning partial glides along the CTB and, thus, causes an increase in the transverse thickness of the twin lamella according to the following reaction:

$$\underbrace{\frac{a}{6}[21\bar{1}]}_{\text{Leading partial}} \rightarrow \underbrace{\frac{a}{6}[\bar{2}11]_T}_{\text{Twinning partial}} + \underbrace{\frac{a}{3}[010]}_{\text{Stair rod dislocation}} \quad , \tag{2}$$

which is illustrated in the double Thompson tetrahedra in Figure 5d with dashed lines and also summarized in Table 2. The GSFE curve for the twinless case is shown in Figure 6a. The GPFE for the incorporation process in the [010] and [111] loading cases are shown in Figure 6b and discussed in the next section. The transmission following incorporation energies are given in Figure 6c.

The configuration that Equation (2) represents is referred to as an i-lock [36]. When the trailing partial $\frac{a}{6}[121]$ reacts with the stair rod, this causes nucleation of a glissile partial penetrating the twin and a Frank partial dislocation at the intersection (see Figure 5c). This can be summarized as follows (also shown in Figure 5d as a dashed line and depicted in Table 2):

$$\underbrace{\frac{a}{3}[010]}_{\text{Stair rod}} + \underbrace{\frac{a}{6}[121]}_{\text{Trailing Partial}} \rightarrow \underbrace{\frac{a}{6}[121]_T}_{\text{Glissile Dislocation}} + \underbrace{\frac{a}{6}[1\bar{1}1]_T}_{\text{Frank Dislocation}} \quad . \tag{3}$$

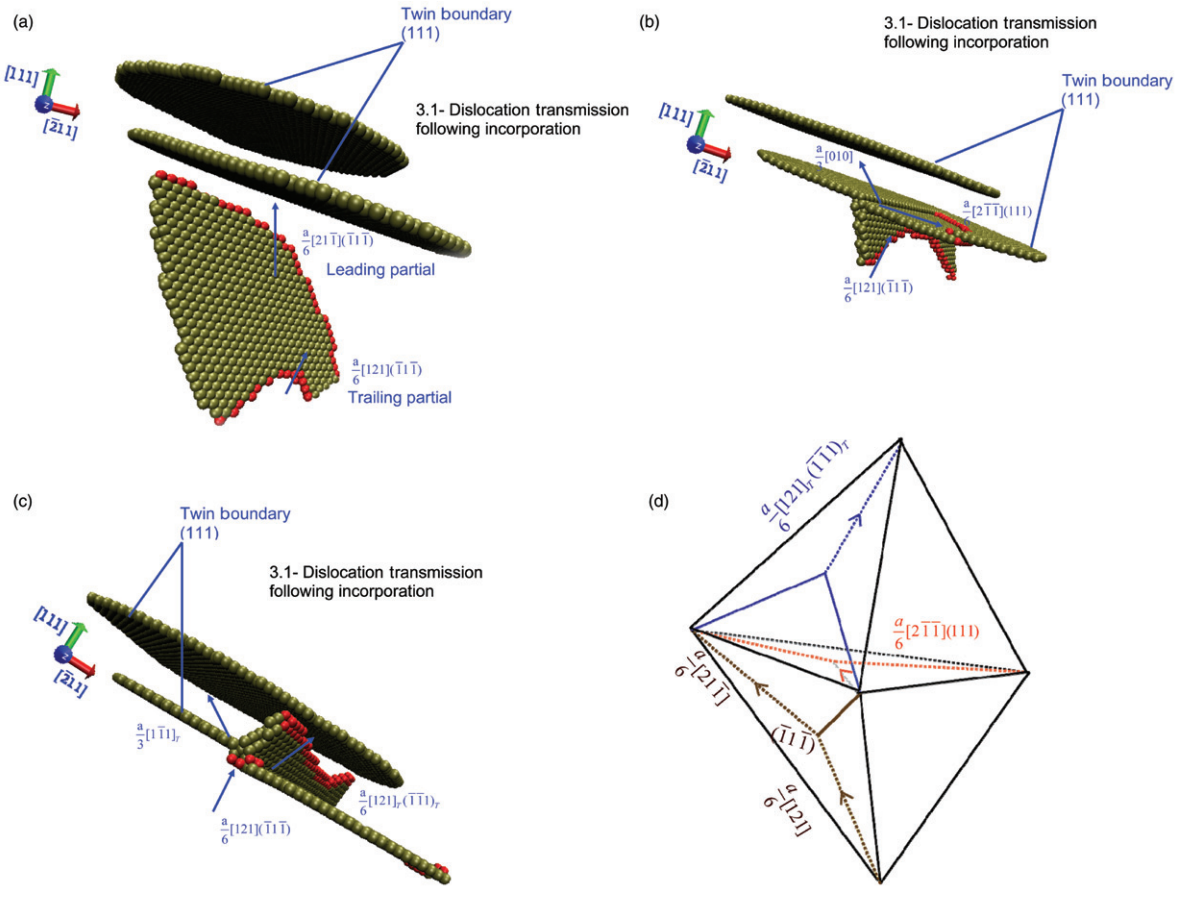

Figure 5. Dislocation–twin boundary interaction for the [010] loading direction in tension. (a) Impinging 60° dislocation with a $\frac{a}{6}[21\bar{1}]$ 30° leading and $\frac{a}{6}[121]$ 90° trailing partial dislocation glides through the matrix before interaction. The deformation twin boundary is $\frac{a}{6}[2\bar{1}\bar{1}](111)$ type. (b) After the leading partial interacts with the twin boundary, a twinning partial $\frac{a}{6}[2\bar{1}\bar{1}]$ and a sessile stair-rod $\frac{a}{3}[010]$ nucleate at the intersection (Case (i)). (c) The dislocation moves to the twinned region in the $\frac{a}{6}[121]_T(\bar{1}\bar{1}1)_T$ system once the trailing partial interact with the boundary (Case (ii)). The view points are slightly varied for a clearer comprehension of the event. (d) Double Thompson tetrahedron, illustrating all the partials involved during the reaction.

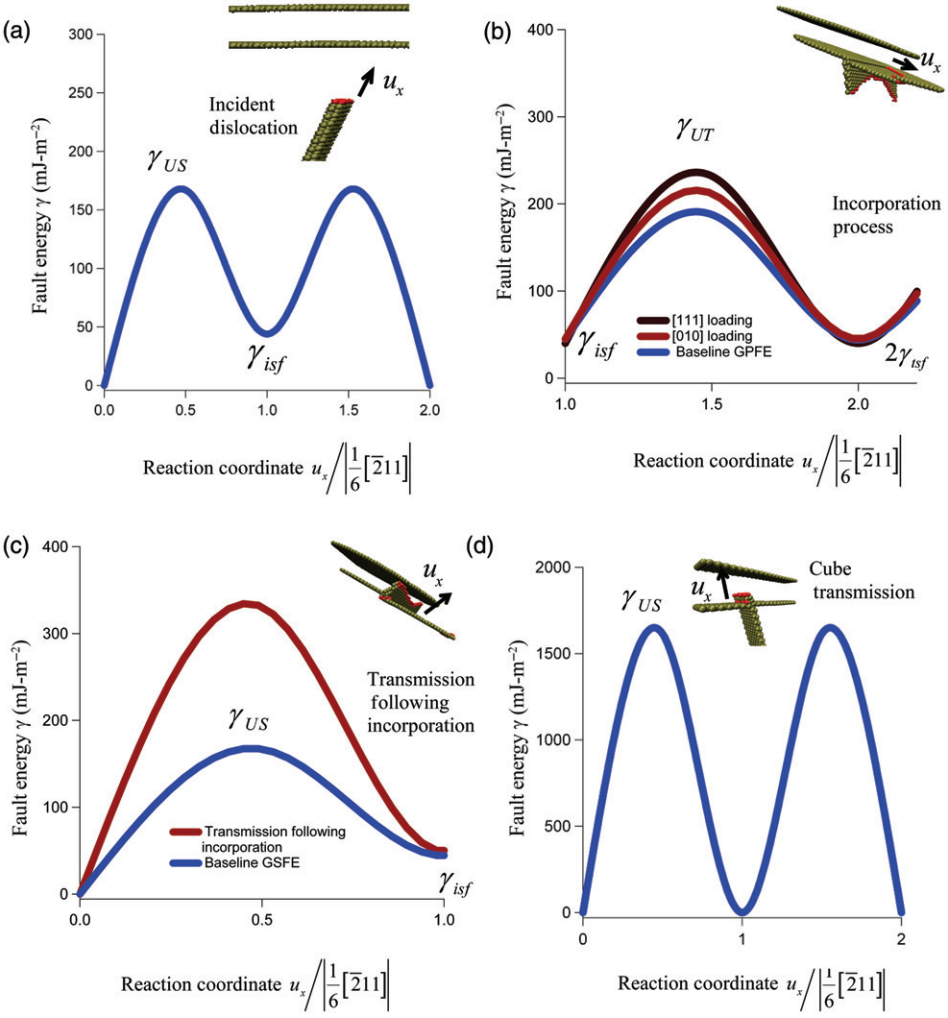

Figure 6. (a) Baseline GSFE curve along $\frac{a}{6}\langle\bar{2}11\rangle$ direction in $\{111\}$ plane for incident dislocation. (b) GPFE curve along $\frac{a}{6}\langle\bar{2}11\rangle$ direction on the $\{111\}$ plane for the twinning partial in the incorporation process during [010] and [111] loading orientation (Case (i)). (c) GSFE curve of transmission of the partial inside the twin after an incorporation process along the $\frac{a}{6}\langle\bar{2}11\rangle$ direction on the $\{111\}$ plane in the [010] loading orientation (Case (ii)). (d) GSFE curve along the $\frac{a}{2}[110]$ direction in the (100) plane for cube transmission in the [111] loading orientation (Case (iii)). (e) GSFE curve along the $\frac{a}{6}\langle\bar{2}11\rangle$ direction on the $\{111\}$ glide plane measured near a Lomer dislocation in [111] loading (Case (iv)). (f) GSFE curve for the nucleated partials at the twin boundary during multiplication event in the [321] loading orientation (Case (v)); one of the dislocations is remitted to the matrix and the other into the twin.

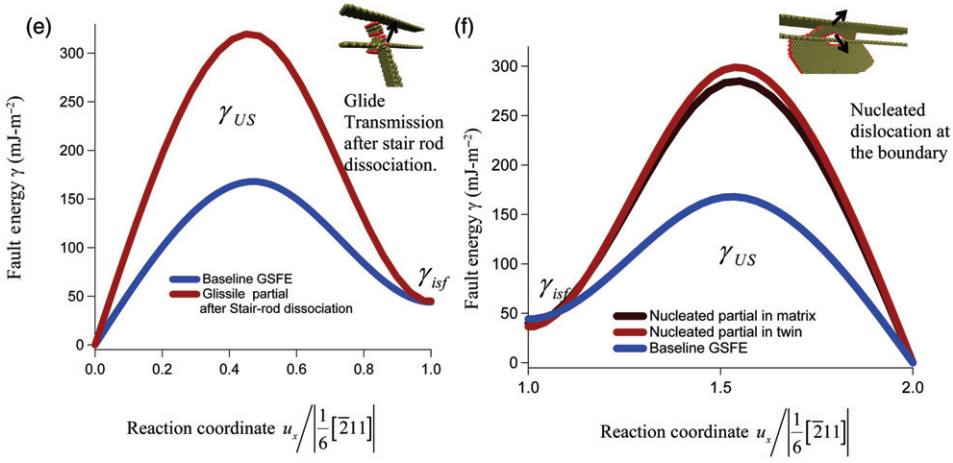

Figure 6. Continued.

The $\frac{a}{6}[121]_T$ penetrates the twin as it glides on the $(111)_T$ plane. The Frank dislocation (Equation (3)) is a sessile imperfect dislocation and its Burgers vector is directed normal to the {111} plane. In Figure 6c (Case (ii)) the elevation of the unstable energies for the transmission within the twin ($\frac{a}{6}[121]_T$) are particularly noteworthy.

3.2. *Incorporation and dislocation blockage at the CTB*

A [111] tensile loading orientation results in dislocation incorporation in the twin but no transmission. Only the leading partial is observed in this orientation as noted in Figure 7a. The leading partial glides on the $(\bar{1}\bar{1}1)$ plane in the $\frac{a}{6}[112]$ direction creating an angle of 30° with the line of intersection. The leading partial has both a screw and an edge component, where the screw component is of $\frac{a}{4}[101]$ type and the edge component is $\frac{a}{12}[\bar{1}21]$. The non-screw component, upon impinging at a $(1\bar{1}\bar{1})[\bar{1}\bar{2}1]$ CTB, nucleates a twinning dislocation along the CTB, which increases the twin lamella by one layer. In the process, a stair rod dislocation is generated according to (illustrated in Figure 7a; Case (i)):

$$\underset{\text{Leading partial}}{\frac{a}{6}[112]} \rightarrow \underset{\text{Twinning partial}}{\frac{a}{6}[12\bar{1}]} + \underset{\text{Stair rod dislocation}}{\frac{a}{6}[0\bar{1}3]} \quad . \tag{4}$$

Note that nucleation of a $\frac{a}{6}[0\bar{1}3]$ stair rod makes an acute angle with the CTB, different than the $\frac{a}{3}[010]$ case discussed earlier. The stair rod dislocation does not dissociate and remains sessile at the interaction site, as illustrated in Figure 7a. The lock produced in this way is also termed an "i-type" twin lock or "i-lock" (same as the earlier definition and Table 2).

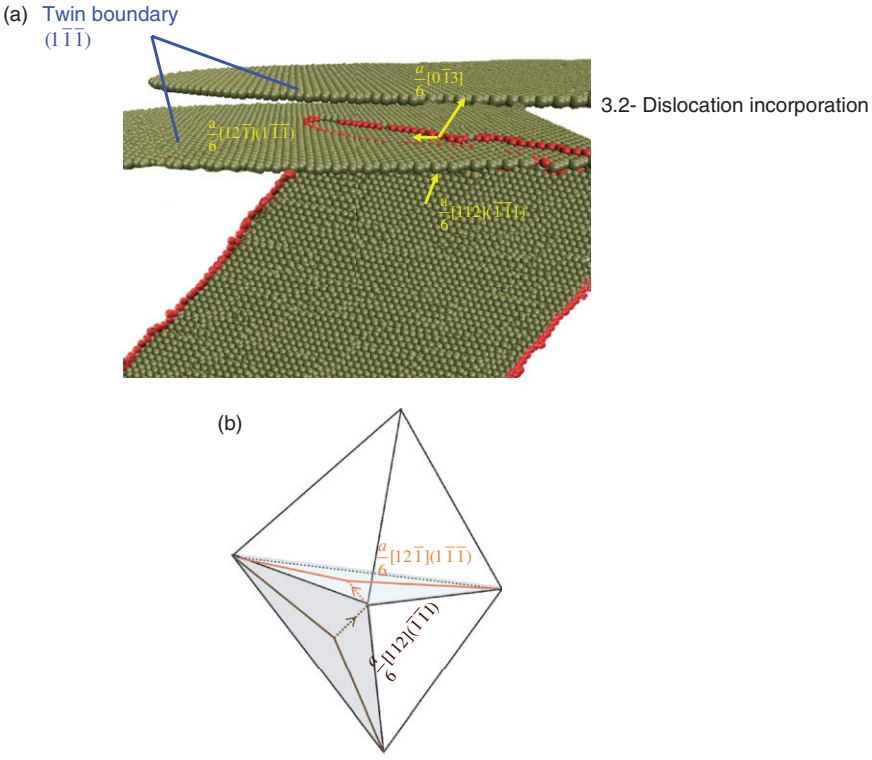

Figure 7. (a) Dislocation–deformation twin boundary interaction for the [111] loading direction in tension (Case (i)). The incident 30° dislocation interacts with a deformation twin boundary creating a twinning partial $\frac{a}{6}[12\bar{1}]$ and a sessile stair-rod $\frac{a}{6}[0\bar{1}3]$ nucleates at the intersection. No trailing partial is observed for this loading as the trailing partial remains pinned in the dislocation source throughout the deformation. (b) Incident and twinning partials are shown in the double Thompson tetrahedron.

Figure 6b displays the energy barrier the twinning partial has to overcome in the [111] loading orientation. The γ_{UT} of magnitude 232 mJ m^{-2} was obtained for this loading orientation, which is higher than the [0101] case and the baseline γ_{UT} levels. This difference in magnitude has an important implication on the hardening behavior of the material as it indicates a higher barrier in nucleating twinning partials for the [111] orientation than the [010] orientation.

3.3. *Lomer dislocation generation and glide plane transmission*

For a similar [111] tension crystal loading orientation, as discussed in Section 3.2, an entirely different interaction mechanism is observed when a different type of dislocation interacts with a CTB of lower Schmid factor (i.e. a non-deformation twin). The incident dislocation for this reaction is a 90° leading partial, which glides in the [211] direction on the (1$\bar{1}\bar{1}$) plane. The trailing partial is again pinned at the source and not observed throughout the loading for this case (Figure 8a);

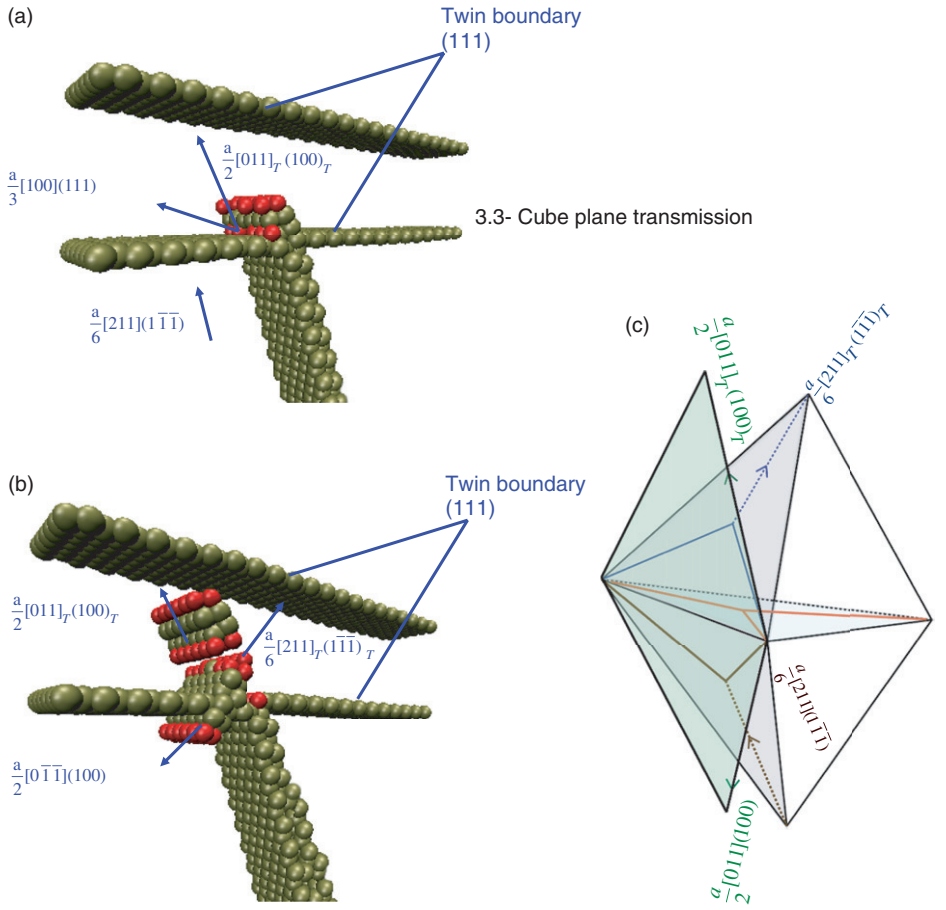

Figure 8. Dislocation–non-deformation twin boundary interaction for the [111] loading direction in tension (Case (iii)). (a) Incident edge dislocation interacts with a non-deformation twin boundary, which creates a Lomer dislocation $\frac{a}{2}[011]_T(100)_T$ and a sessile stair-rod $\frac{a}{2}[101]$ dislocation nucleates at the intersection. No trailing partial is observed for this loading as the trailing partial remain pinned in the dislocation source throughout the deformation. (b) $\frac{a}{3}[101]$ stair-rod finally dissociates into two more glissile dislocation, one in twinned region of type $\frac{a}{6}[211]_T(1\bar{1}\bar{1})_T$ and the other $\frac{a}{2}[0\bar{1}\bar{1}](100)$ in matrix region. (c) Double Thompson tetrahedron illustrating all the dislocations involved during the reaction. The cube $(100)_T$ plane is also shown with the tetrahedron which makes an angle of 125° with the (111) twin boundary plane.

thus, the trace of the intrinsic stacking fault is always visible behind the leading partial. However, the dislocation impinges on the $(111)[\bar{2}11]$ CTB with zero Schmid factor for this loading orientation. The incident partial, once it reacts with this CTB, nucleates a Lomer type dislocation at the intersection, which glides in the twinned region in the $[011]_T$ direction. This is illustrated in Figure 8b, Case (iii). Rather than gliding in the regular slip plane, this Lomer-type dislocation glides in the $(100)_T$ cube plane. As the 90° partial is of edge character, once it reacts with the CTB, it creates a jog at the intersection site. This jog produces an

additional step at the intersection and no twinning partial is observed at the CTB. In fact, the Schmid factor for the non-deformation CTB is not favorable for twin partial nucleation in this orientation. Hence, an impinging partial dislocation at the CTB creates a Lomer dislocation and a stair rod dislocation of $\frac{a}{3}[100]$ type. The slip transfer across the CTB is shown in Figure 8a and can be expressed as follows:

$$\underset{\text{Leading partial}}{\frac{a}{6}[211]} \rightarrow \underset{\text{Lomer dislocation}}{\frac{a}{2}[011]_T} + \underset{\text{Stair rod dislocation}}{\frac{a}{3}[100]} \quad . \tag{5}$$

This $\frac{a}{3}[100]$ stair rod dislocation, however, is not stable and further dissociates into new dislocations:

$$\underset{\text{Stair rod dislocation}}{\frac{a}{3}[100]} \rightarrow \underset{\text{Remitted Lomer dislocation}}{\frac{a}{2}[0\bar{1}\bar{1}]} + \underset{\text{Stair rod dislocation}}{\frac{a}{6}[233]} \quad , \tag{6}$$

which is illustrated in Figure 8b. The (100) plane in a fcc material is not a closed packed plane; hence, the unstable stacking fault energy barrier in this cube plane is significantly higher than the conventional (111) glide plane. We calculated this energy barrier as 1614 mJ m^{-2} as illustrated in Figure 6d. The dissociation of the $\frac{a}{6}[233]$ results in an $\frac{a}{6}[211]_T$ that nucleates and glides within the twinned region on the regular $(1\bar{1}\bar{1})_T$ plane as seen in Figure 8b. The reaction process of these two dislocations can be summarized as follows:

$$\underset{\text{Stair rod dislocation}}{\frac{a}{6}[233]} \rightarrow \underset{\text{Leading partial}}{\frac{a}{6}[211]_T} + \underset{\text{Frank Partial dislocation}}{\frac{2a}{9}[111]} \quad . \tag{7}$$

The reactions are reviewed in Table 2 and also illustrated in Figure 8c, Case (iii). A unique feature of this mechanism is dislocation multiplication. The dislocation reaction at the CTB gives rise to three dislocations while leaving the boundary intact. The a/6[233]-type dislocation is a sessile dislocation and is not observed experimentally. This is partly because this dislocation is energetically highly unstable, and immediately breaks down into two more dislocations as noted above. On the other hand, we note that the 2a/9[111]-type dislocations have been observed in experiments [23,24].

The Schmid factor of the CTB has a significant influence in the twin–slip interactions. In addition to that, the GSFE curve for glide transmission inside the twin demonstrates the presence of a high stress field both for stair rod dissociation and the presence of a Lomer dislocation discussed above. The γ_{US} of 314 mJ m^{-2} (Figure 6e) for $\frac{a}{6}[\underline{2}11]_T$ indicates a much higher energy barrier compared to the incident $\langle 211\rangle\{1\bar{1}\bar{1}\}$ system (Figure 6a). This magnitude, however, decreases once the partial moves away from the interaction site and reduces to 210 mJ m^{-2}.

3.4. *CTB translation, growth and contraction*

Upon loading in the [321] or the [101] tension orientations in the presence of deformation twins, coplanar twinning dislocations glide at the CTB. This behavior is

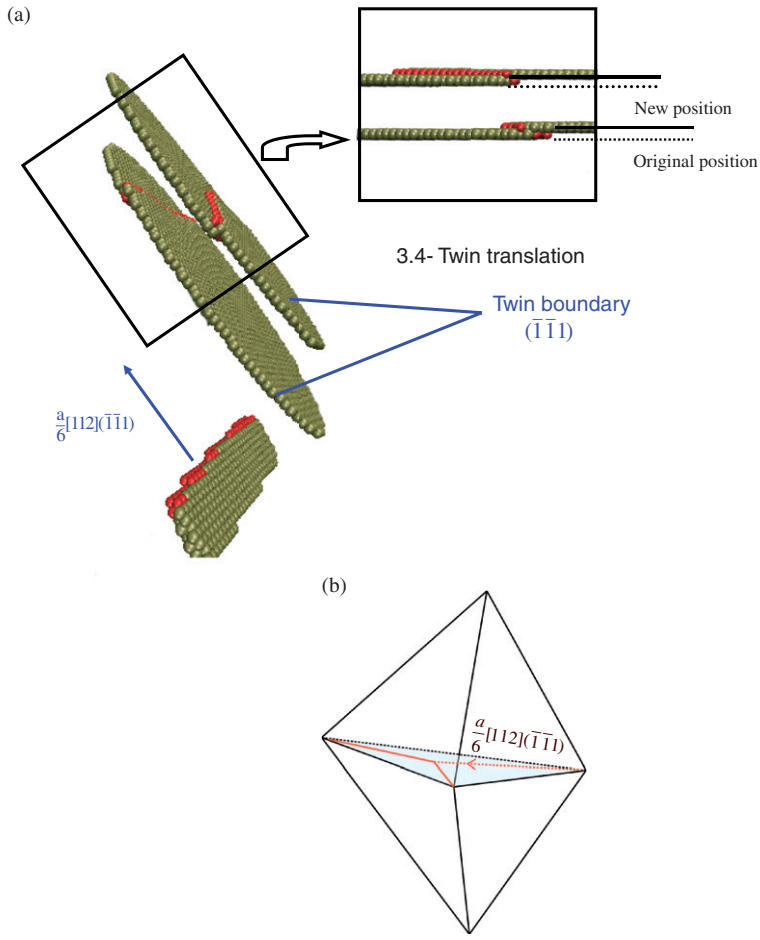

Figure 9. (a) Coplanar dislocation with a deformation twin boundary loaded in the [321] crystal orientation in tension as only one system is activated in this loading direction (Case (iv)). The twinning partial is nucleated at both the twin boundaries. The solid line shows the new position of the twin boundary, since the dislocation glides and causes twin migration by one Burgers vector from the original position shown by the dotted line. (b) Traversing twinning partials shown in a double Thompson tetrahedron.

anticipated in view of the limited systems activated in these two cases. The leading partial nucleating from the source is in the same system as the deformation CTB and, consequently, no interaction is expected. In the case, when the source is one of the twin boundaries, the twin lamella grows or contracts by one layer depending upon the direction of the dislocation motion. At high strains, the partials nucleate at the same end of both the boundaries and glide in the same direction, which causes a rigid body translation of the CTB by one layer as shown in Figure 9a, Case (iv). The Thompson tetrahedron representation is given in Figure 9b.

In case of the [101] loading direction, the twinning partials are nucleated from opposite ends; the twin lamella thickens or contracts by two layers depending on

the glide direction of the twinning partial. Twinning partial glides in this case in the $[\bar{1}\bar{1}2](111)$ and $[11\bar{2}](\bar{1}\bar{1}\bar{1})$ directions in upper and lower CTB, respectively. As these two directions are mutually opposite in nature, this thickens the twin by two layers. However, if nucleation and glide of these partials are opposite, i.e. if dislocations glide in $[11\bar{2}](\bar{1}\bar{1}\bar{1})$ and $[\bar{1}\bar{1}2](111)$ directions in the upper and lower CTB, the twin would contract by two layers. The energetics for this case corresponds to the relaxed curve in Figure 6b. The growth and translation processes can be observed in [010] and [111] tension as well. However, a higher number of activated systems dominate in these cases leading to the interactions as discussed earlier.

3.5. *Glide plane transmission of dislocation at the CTB*

A material volume with a non-deformation twin is subjected to the [321] tension loading orientation. In this case, the incident dislocation encounters a CTB with a low Schmid factor. This behavior differs from a CTB with the maximum Schmid factor (studied in Section 3.4). A 30° leading partial dislocation nucleates from the source during deformation and glides in the [112] direction on the $(\bar{1}\bar{1}1)$ glide plane. In this crystal loading orientation, the trailing partial does not have a significant a role. The incident mixed dislocation, once reacted with the CTB, continues to form a larger dislocation segment in the reacting [011] line direction at the intersection, as shown in Figure 10a, Case (v). At this segment, a 30° partial nucleates within the CTB in the form of a loop. During this reaction, a Frank partial is created at the CTB:

$$\underset{\text{Leading partial in matrix}}{\frac{a}{6}[112]} \rightarrow \underset{\text{Leading partial in twin}}{\frac{a}{6}[121]_T} + \underset{\text{Frank partial}}{\frac{2a}{9}[\bar{1}11]} \ . \tag{8}$$

The motion of the leading partial in the twin undergoes an energy barrier elevated from that of a twin-free matrix.

The Frank partial, which is directed normal to (111) plane, is unstable and further dissociates into two more partials – one glides in the twinned region and the other partial is reemitted in matrix (see Figure 10b and Table 2).

$$\underset{\text{Frank Partial}}{\frac{2a}{9}[\bar{1}11]} \rightarrow \underset{\text{Trailing Partial in Twin}}{\frac{a}{6}[21\bar{1}]_T} + \underset{\text{Reemitted Partial in Matrix}}{\frac{a}{6}[\bar{2}1\bar{1}]} \tag{9}$$

The $\frac{a}{6}[\bar{2}1\bar{1}]$ partial, upon reemission, removes the stacking fault left by the leading partial. The energetics of this case is given in Figure 6f, corresponding to the trailing partial in the twin and the reemitted partial in the matrix. It is shown that the barriers for glide through a CTB are significantly higher compared to a regular dislocation glide case (Figure 6a) supporting a significant level of strengthening associated with non-deformation twins. The reemission behavior of an incident dislocation from a CTB is reported experimentally [50]; in this study, we provide the associated energy barrier.

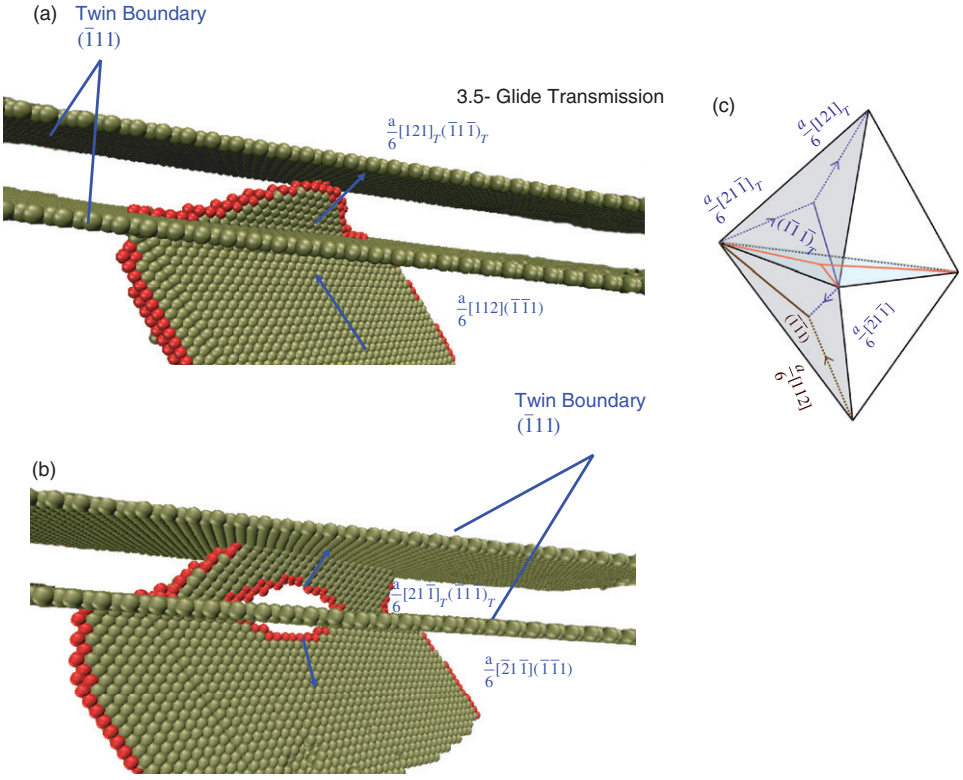

Figure 10. Dislocation–non-deformation twin boundary interaction for the [321] loading direction in tension (Case (v)). (a) The incident 30° partial dislocation $\frac{a}{6}[211](\bar{1}11)$ interacts with a non-deformation twin boundary, which creates a partial dislocation $\frac{a}{6}[121]_T(\bar{1}1\bar{1})_T$ and a sessile Frank dislocation $\frac{2a}{9}[\bar{1}11]$ at the intersection. No trailing partial is observed for this loading as the trailing partial remains pinned in the dislocation source throughout the deformation. (b) A $\frac{2a}{9}[\bar{1}11]$ Frank partial dissociates into two more glissile dislocation and causes a dislocation multiplication. One dislocation glides in the twinned region, which acts as a trailing partial of $\frac{a}{6}[21\bar{1}]_T(\bar{1}1\bar{1})_T$ type, and the other partial dislocation $\frac{a}{6}[\bar{2}1\bar{1}](\bar{1}\bar{1}1)$ glides and annihilate the partial dislocation left by the original incident dislocation $\frac{a}{6}[112](\bar{1}\bar{1}1)$. (c) Double Thompson tetrahedron illustrating the dislocations involved during the reaction.

4. Discussion of results

The simulations determined precisely the energetics of slip–twin interactions under tensile deformation, particularly in the presence of sessile dislocations. The twin boundaries serve as effective barriers in all cases, but the energy barriers are higher in some crystal orientations than others. Compared to dislocation glide in the perfect lattice, the glide of partials along twin boundaries (incorporation) requires crossing a higher energy barrier. This is clearly illustrated in Figure 6b. Transmission following incorporation also faces a high-energy barrier as illustrated in Figure 6c. Glide transmission near a Lomer dislocation (Figure 6d) requires surmounting higher energy barriers hence considerable strengthening can occur in these cases. Dislocation multiplication at the CTB (Figure 6f) and transmission near a Frank

dislocation (Figure 6e) also produce substantial elevations in the planar fault energy curves. Twin translation with coplanar slip provides the least effective barrier to slip among all cases. We note that, all these five different dislocation–CTB reaction cases (Cases (i)–(v)) have been observed previously in experimental research [12,14,16–21,24–26,30,31].

The results clearly point to the role of loading orientation and Schmid factor on dislocation–CTB interactions. A classification of these interaction mechanisms into different categories and identifying the energy barriers for slip is achieved in this work. This improves the current understanding of strain-hardening behavior of low SFE materials as a function of crystallographic orientation. Orientations near the [111] pole of the stereographic triangle are expected to provide the highest resistance to slip, as a consequence are hard orientations. In this case, glide transmission near a Lomer dislocation is associated with high energy barriers. The residual dislocations encountered in the [111] and the [010] loading cases elevate the energy barrier associated with incorporation. The presence of deformation twins for loading orientations near the [101] pole and near the [321] (inside the stereographic triangle) also provide resistance to flow but to a lesser extent than the [111] and [010] cases.

These simulations on the orientation dependence of strain hardening are in agreement with the significant amount of experimental evidence obtained on deformation of single crystals with twins [2–4,6–8]. In these studies, there have been significant emphases on the magnitude of the intrinsic stacking fault energy and its role in strengthening. The present study points to the considerable elevation of the unstable twin and unstable stacking fault energies. For example, the simplified twinning stress equation proposed in our earlier work [45] for twin nucleation and early growth points to a stronger dependence on the unstable twin energy (relevant to incorporation) compared to the intrinsic stacking fault energy We also note that based on the earlier work of Rice [36], the nucleation stress increases proportional to the unstable fault energy to a first approximation. Hence, any increase in unstable fault energy would require an increase in the stress magnitudes for slip motion.

The results are consistent with the early works of Mahajan [18], Remy et al. [13], Hartley et al. [10] and, recently, by Jin et al. [51] on the incorporation process and that of Robertson [52] regarding the choice of active systems at CTBs. Robertson et al. [52] proposed three criteria to predict which system is activated after the intersection. These criteria were developed initially for full dislocations; our results show that these criteria hold for partial dislocations interacting with CTB as well. The first is a geometric criterion, which ensures that the angle between the line of intersection at the boundary of the incoming and outgoing dislocation is minimized. In all our results, this angle is zero, as expected for the CTBs, which is the absolute minimum. Also, our results satisfy the second condition, which requires a maximum value of the resolved shear stress acting on the outgoing slip system. The third criterion requires the residual boundary dislocation be a minimum. Our analyses reveal that in all the cases, residual dislocations are created either in the form of a stair rod or Frank dislocation with different Burgers vector magnitudes. We note that the internal stress fields associated with these residual dislocations elevate the unstable fault energies and contribute to the strengthening associated with CTBs.

The loading orientation influences dislocation–CTB interactions in three ways. It affects the critical resolved shear stress factor of the CTB, influences dislocation separation distance determined by the stacking fault energy and determines the screw and edge components of the incident dislocation. For example, in the [111] loading orientation, no trailing partial is observed (in Cu) and this prevents further dissociation of the sessile dislocations at the boundary, leading to further hardening as observed in our case. Apart from the orientation dependence [9,53], the γ_{isf}/γ_{US} ratio is a factor in deciding the presence of the trailing partial [54]. Lower ratios favor higher separation distances such that the leading partial plays a major role in interactions with CTBs. We expect that other low stacking fault energy metals to behave similarly to copper.

The i-locks formed at the dislocation–CTB junction trap incoming dislocations to form dislocation pileups at the twin boundaries. In addition to i-lock formation in the [111] loading orientation, a glissile Lomer dislocation is also observed in this orientation when the incident dislocation interacts with a non-deformation twin. The value of γ_{US} for a Lomer dislocation is found to be $1614\,\mathrm{mJ\,m^{-2}}$, which is significantly higher than that of the normal glide plane ($167\,\mathrm{mJ\,m^{-2}}$). Hence, its translation is confined to a short distance across the twin transverse direction. The flow proceeds upon a stair rod disassociation, which leads to a Frank partial and glide transmission with significant elevation of the unstable energy levels (Figure 6e).

The unrelaxed energy curves represent the role of internal stress fields on the energy barrier [42]. The unrelaxed and relaxed baseline GPFE curves in Figure 6b illustrate the energy barriers that the twinning partials must overcome in an incorporation process after forming the i-lock in the [010] and the [111] loading orientations, respectively. A relaxed GPFE signifies the energy barrier for dislocation nucleation in the stress-free state similar to the simulations conducted in our earlier work using density functional theory [45]. The increase in magnitude of γ_{UT} was measured as 47 and $27\,\mathrm{mJ\,m^{-2}}$ for the [111] and the [010] loading orientations, respectively. This increase in energy barrier is attributed to the local stress field generated, due to the presence of sessile stair-rod dislocation at the interaction site. In both of these loading directions, the stair-rod dislocations create an angle of 54° with the CTB. In the [010] loading direction, the magnitude of stair-rod dislocation is $0.33a$, whereas in the [111] orientation, it is found to be $0.527a$. Thus, this difference in energy barrier explains the efficacy of the residual dislocation in the hardening process as observed experimentally [52]. These results provide an additional rationale for higher strain-hardening behavior observed in the [111] orientations in fcc metals [55] and alloys [2,56–58]. Unlike stair-rod dislocations, a Frank partial dislocation creates an angle of 90° with the close packed planes. Hence, the Frank partial dislocation generates a much higher local stress concentration at the barrier. This is reflected in the increase of γ_{US} of the nucleated dislocation at the boundary by $158\,\mathrm{mJ\,m^{-2}}$ (from baseline γ_{us}) in Figure 6f and by $178\,\mathrm{mJ\,m^{-2}}$ in Figure 6c.

Also, our results clarify the lower hardening observed in the [321] and the [101] tension crystal orientation in the presence of deformation twins. After the nucleation of a deformation twin, additional dislocation-twin interactions are limited in the [321] and [101] cases, due to the coplanar nature of the dislocation with the deformation twin. Twin migration and twin growth (or shrinkage) is observed in

these loading cases as CTB motion has a strong dependency on the shear direction along CTB [35]. Migration or growth (shrinkage) only occurs for the deformation twin in the [321] and the [101] loading orientation, as this enforces a maximum shear stress in the $\langle 11\bar{2}\rangle\{111\}$ direction along the CTB. For the non-deformation case in the [321] loading orientation, the maximum shear is in the $\langle \bar{1}01\rangle\{111\}$ direction and no migration or growth (shrinkage) is expected. TEM images in low SFE materials [2,4] verify these results in these loading orientations. On the other hand, the results point to the possibility that a non-deformation twin with a low Schmid factor may be a source of dislocation multiplication (Figures 10a and b). This is observed in both the [111] and [321] loading orientations. In this case, one of the nucleated dislocations at the CTB is reemitted to the matrix region (with a high energy barrier (Figure 6f), thus annihilating the stacking fault that trails the leading incident partial.

In summary, in the calculation of GPFE, all fault energies are determined relative to the energy of the fcc structure under the same external stress. Overall, the results point to a significant contribution of the internal stresses on the energy barriers and ultimately the reaction-induced (complex) stress states at the twin boundaries, which govern the resulting dislocation glide behavior.

5. Conclusions

The present work extends our understanding of the role of crystal loading direction on dislocation–CTB interactions, introduced a novel technique for tracking energy barriers during deformation, and provided a rationale for CTB strengthening in fcc crystals. The results support the following conclusions:

(1) The results provide quantitative evidence of enhanced energy barriers in twin–slip interactions and prove that twins are strong barriers to dislocation glide in fcc metals. The results point to the exact interaction that occurs under the given loading conditions among a wide range of slip–twin interactions. The work addresses a number of cases that have been observed experimentally, but have not received wide attention, and also introduces previously unreported reactions and multiplication cases.

(2) Dislocation reemission in the matrix, glide at the CTB or inside the twin present varying energy barriers that decide the strengthening in fcc metals undergoing slip–twin interactions. Lomer, stair-rod, and Frank partial dislocations are nucleated during dislocation–CTB interactions with varying dislocation vectors, which modify the local stress fields and elevate the energy barriers for glide in the matrix and in the twin. The conditions under which these residual dislocations occur are determined precisely in this paper. The work extends previous treatments by providing a unifying 'energy barrier' framework to understand all possible interactions and reactions.

(3) Under [111] tensile loading, a considerably higher energy barrier has been observed under various scenarios including incorporation and short-range cube transmission of the leading partial dislocation. A modest amount of hardening is expected in the [010] case with the incident dislocation undergoing incorporation and transmission. The lack of multiple slip and deformation twin systems in the [321] and [101] tension orientations causes

coplanar dislocations resulting in twin growth, contraction, or rigid body translation with modest effects on strain hardening. Interestingly, the non-deformation twins, resulting in Frank partials in the [321] case, can be very effective in elevating the energy barriers for dislocation multiplication and reemission.

Acknowledgements

The research was supported by the National Science Foundation, Virginia, USA, Division of Materials Research, through Grant No. 0803270.

References

[1] T.H. Blewitt, R.R. Coltman and J.K. Redman, J. Appl. Phys. 28 (1957) p.651.
[2] Y.I. Chumlyakov, A.M. Li and A.D. Korotayev, Phys. Met. Metallogr. (USSR) 62 (1986) p.164.
[3] V.A. Levin, Y.I. Chumlyakov, N.V. Nikitina and A.D. Korotayev, Phys. Met. Metallogr. 68 (1989) p.155.
[4] I. Karaman, H. Sehitoglu, K. Gall, Y.I. Chumlyakov and H.J. Maier, Acta Mater. 48 (2000) p.1345.
[5] C. Efstathiou, H. Sehitoglu, Acta Mater. 51 (2010) p.1479.
[6] A.D. Korotayev, V.F. Yesipenko, Y.I. Chumlyakov, L.S. Bushnev and Y.G. Veselov, Phys. Met. Metallogr. 55 (1983) p.133.
[7] A.D. Korotaev, Y.I. Chumlyakov, L.S. Bushnev, Y.G. Veselov, V.F. Esipenko and V.N. Lineitsev, Fizika Metallov i Metallovedenie 50 (1980) p.406.
[8] Z.K. Khamitov, Y.I. Chumlyakov and A.D. Korotaev, Fizika Metallov i Metallovedenie 68 (1989) p.177.
[9] S. Copley and B.D. Kear, Acta Metall. 16 (1968) p.227.
[10] C.S. Hartley and D.L.A. Blachon, J. Appl. Phys. 49 (1978) p.4788.
[11] R.J. Asaro and Y. Kulkarni, Scripta Mater. 58 (2008) p.389.
[12] P. Müllner and C. Solenthaler, Mater. Sci. Eng. A 230 (1997) p.107.
[13] L. Rémy, Metal. Mater. Trans. A 12 (1981) p.387.
[14] G. Vellaikal, Acta Metall. 17 (1969) p.1145.
[15] T. Zhu, J. Li and S. Yip, Phys. Rev. Lett. 93 (2004) p.025503.
[16] J.T. Evans, Scripta Metall. 8 (1974) p.1099.
[17] K. Saito, Natl. Res. Inst. Met. 27 (1969) p.1234.
[18] S. Mahajan and G.Y. Chin, Acta Metall. 21 (1973) p.173.
[19] L. Remy, Scripta Metall. 11 (1977) p.169.
[20] J.A. Venables, in *Deformation Twinning*, R.E. Reed-Hill, J.P. Hirth and H.C. Rogers, eds., Gordon Breach, New York, 1964, p.77.
[21] L.C. Lim, Scripta Metall. 18 (1984) p.1139.
[22] T. Zhu, J. Li, A. Samanta, H.G. Kim and S. Suresh, Proc. Natl. Acad. Sci. USA 104 (2007) p.3031.
[23] D.L. Medlin, C.B. Carter, J.E. Angelo and M.J. Mills, Phil. Mag. A 75 (1997) p.733.
[24] R.C. Pond and V. Vitek, Proc. R Soc. A 357 (1977) p.445.
[25] H.P. Karnthaler, Phil. Mag. 38 (1978) p.141.
[26] A. Korner and H.P. Karnthaler, Phys. Status Solidi A 75 (1983) p.525.
[27] F. Sansoz, H. Huang and D. Warner, JOM. J. Miner. Met. Mater. S 60 (2008) p.79.
[28] J. Wang and H. Huang, Appl. Phys. Lett. 88 (2006) p.203112.

[29] S. Mahajan, D.E. Barry and B.L. Eyre, Phil. Mag. 21 (1970) p.43.
[30] V.S. Boiko, Sov. Phys. Solid State 22 (1980) p.621.
[31] S.V. Lubenets and L.S. Fomenko, Kristall Technik 13 (1978) p.1325.
[32] Y.B. Wang, M.L. Sui and E. Ma, Phil. Mag. Lett. 87 (2007) p.935.
[33] D.P. Field, B.W. True, T.M. Lillo and J.E. Flinn, Mater. Sci. Eng. A 372 (2004) p.173.
[34] T. Kizuka, Jap. J. Appl. Phys. 46 (2007) p.7396.
[35] H. Qiyang, L. Lan and N.M. Ghoniem, Acta Mater. 57 (2009) p.4866.
[36] Z.X. Wu, Y.W. Zhang and D.J. Srolovitz, Acta Mater. 57 (2009) p.4508.
[37] B. Escaig, J. Phys. (Paris) 29 (1968) p.225.
[38] W.F. Hosford and R.L. Fleischer, Acta Metall. 7 (1959) p.816.
[39] Z.H. Jin, P. Gumbsch, E. Ma, K. Albe, K. Lu, H. Hahn and H. Gleiter, Scripta Mater. 54 (2006) p.1163.
[40] Z. Chen, Z. Jin and H. Gao, Phys. Rev. B 75 (2007) p.212104.
[41] E.O. Hall, *Twinning and Diffusionless Transformations in Metals*, Butterworths, London, 1954.
[42] J.R. Rice, J. Mech. Phys. Solids 40 (1992) p.239.
[43] Y. Mishin, M.J. Mehl, D.A. Papaconstantopoulos, A.F. Voter and J.D. Kress, Phys. Rev. B 63 (2001) p.224106.
[44] R.D. Boyer, J. Li, S. Ogata and S. Yip, Model. Simul. Mater. Sci. 12 (2004) p.1017.
[45] S. Kibey, J.B. Liu, D.D. Johnson and H. Sehitoglu, Acta Mater. 55 (2007) p.6843.
[46] S. Plimpton, J. Comput. Phys. 117 (1995) p.1.
[47] W. Humphrey and A.S.K. Dalke, J. Mol. Graphics 14 (1996) p.33.
[48] C.L. Kelchner, S.J. Plimpton and J.C. Hamilton, Phys. Rev. B 58 (1998) p.11085.
[49] S. Ogata, J. Li and S. Yip, Science 298 (2002) p.807.
[50] B. Miller, J. Fenske, D. Su, C.-M. Li, L. Dougherty and I.M. Robertson, *Grain boundary responses to local and applied stress: an* in situ *TEM deformation study*, Vol. 976, Materials Research Society, Boston, MA, 2006, p.84.
[51] Z.H. Jin, P. Gumbsch, K. Albe, E. Ma, K. Lu, H. Gleiter and H. Hahn, Acta Mater. 56 (2008) p.1126.
[52] I.M. Robertson, T.C. Lee, P. Rozenak, G.M. Bond and H.K. Birnbaum, Ultramicroscopy 30 (1989) p.70.
[53] D. Goodchild, W.T. Roberts and D.V. Wilson, Acta Metall. 18 (1970) p.1137.
[54] H. Van Swygenhoven, P.M. Derlet and A.G. Froseth, Nat. Mater. 3 (2004) p.399.
[55] J. Diehl, Z. Metallk. 47 (1956) p.331.
[56] I. Karaman, H. Sehitoglu, H.J. Maier and Y.I. Chumlyakov, Acta Mater. 49 (2001) p.3919.
[57] Y.I. Chumlyakov and A.D. Korotaev, Russ. Phys. J. 35 (1992) p.783.
[58] A.M. Li, Y.I. Chumlyakov and A.D. Korotaev, Phys. Met. Metallogr. (USSR) 65 (1988) p.174.